

Volume 2, Number 2, pp. 96-117, 2000.

◀ Home Current Issue Table of Contents ▶

Electrical Excitation Propagation in the Human Heart

C. D. Werner, F. B. Sachse and O. Dössel

Institute of Biomedical Engineering, University of Karlsruhe, 76128 Karlsruhe, Germany

Correspondence: cw@ibt.etec.uni-karlsruhe.de

Abstract. This work deals with the simulation of the electrical cardiac excitation propagation based on anatomical models of the human heart and body. The generation of anatomical models applying different techniques of digital image processing to medical image data is described as well as the generation of electrophysiological models based on these anatomical models. Different spatial and temporal physical field distributions, e.g. the transmembrane potential, the current sources and the extracellular potentials, are calculated and visualized in sinus rhythm case as well as in pathological cases.

Keywords: Cardiac Modeling, Excitation Propagation, Bidomain Model, Electrophysiology, Cellular Automaton, Anatomical Models

Introduction

The main function of the heart is to sustain the circulation of blood in the body by pumping oxygenated blood from the left ventricle into the body and deoxygenated blood from the right ventricle into the lungs. This function is provided by the temporal and spatial mechanical deformation of the heart. The deformation itself is strongly coupled to the electrical excitation in the heart. In addition to the impact on the mechanical deformation the electrical excitation propagation is the origin for the evolution of a temporal and spatial distribution of extracellular potential measurable as ECG on the body surface. In many cases, a pathological electrical excitation propagation leads to a pathological mechanical contraction and therefore to a malfunction of the heart. Modeling of the electrical excitation propagation is of permanent interest in basic research in cardiology. At present the research in this field can be divided into two parts: On a cellular level the research is focussed on the development and improvement of cellular models and models of the excitation propagation in cell clusters. The other part is focussed on a macroscopic level of simulation to enable fast calculations on models of the total heart, thorax and body [1]. Different applications may be found in the fields of diagnosis, therapy and medical education in cardiology based on either part of this research field. This work deals with the simulation of the electrical excitation propagation in the human heart based on a cellular automaton and the calculation of current sources and potential distribution in the whole body. The intention is to provide simulation

results fast, if possible in real-time, including the visualization of these results. Nonetheless, they have to be accurate enough to obtain realistic electrocardiograms (ECG). Simulations of the sinus rhythm are demonstrated as well as simulations of different pathological cases. Results of these simulations include various physical field distributions which are visualized as 3D scenarios and animations.

Methods

Modeling the Human Anatomy

Overview

An important task of this work is the computer based modeling of the human anatomy. To obtain a detailed anatomical model, the image data of the Visible Man dataset [2] [3] provided by the National Library of Medicine, Bethesda, Maryland (USA), are processed by means of several techniques of digital image processing. Completing this task a voxel based anatomical model of the human heart and body is created. The voxels describe the location of different types of tissue in space. The size of one voxel is $1 \text{ } mm \times 1 \text{ } mm \times 1 \text{ } mm$. For each voxel classified as cardiac or skeletal muscle the fiber orientation is determined to enable simulations regarding anisotropic properties.

Macroscopic Human Cardiac Anatomy

The human heart basically consists of the left and right atria, and the left and right ventricles. Each of these parts include myocardial tissue surrounding a cavity. The right atrium collects and stores deoxygenated blood from the body. The right atrium adjoins to the right ventricle through the tricuspid valve. The blood of the right ventricle is pumped through the pulmonary arteries passing the pulmonary valve and finally reaches the lungs where it is oxygenated. The left atrium collects and stores the oxygenated blood from the lungs. The border between the left atrium and the left ventricle is the mitral valve. The blood of the left ventricle is pumped through the aorta into the body passing the aortic valves [4][5]. The left and right ventricles are separated by the interventricular septum, the left and right atria by the interatrial septum. A cross section of a human heart is shown in Figure 1, a 3D view in Figure 2.

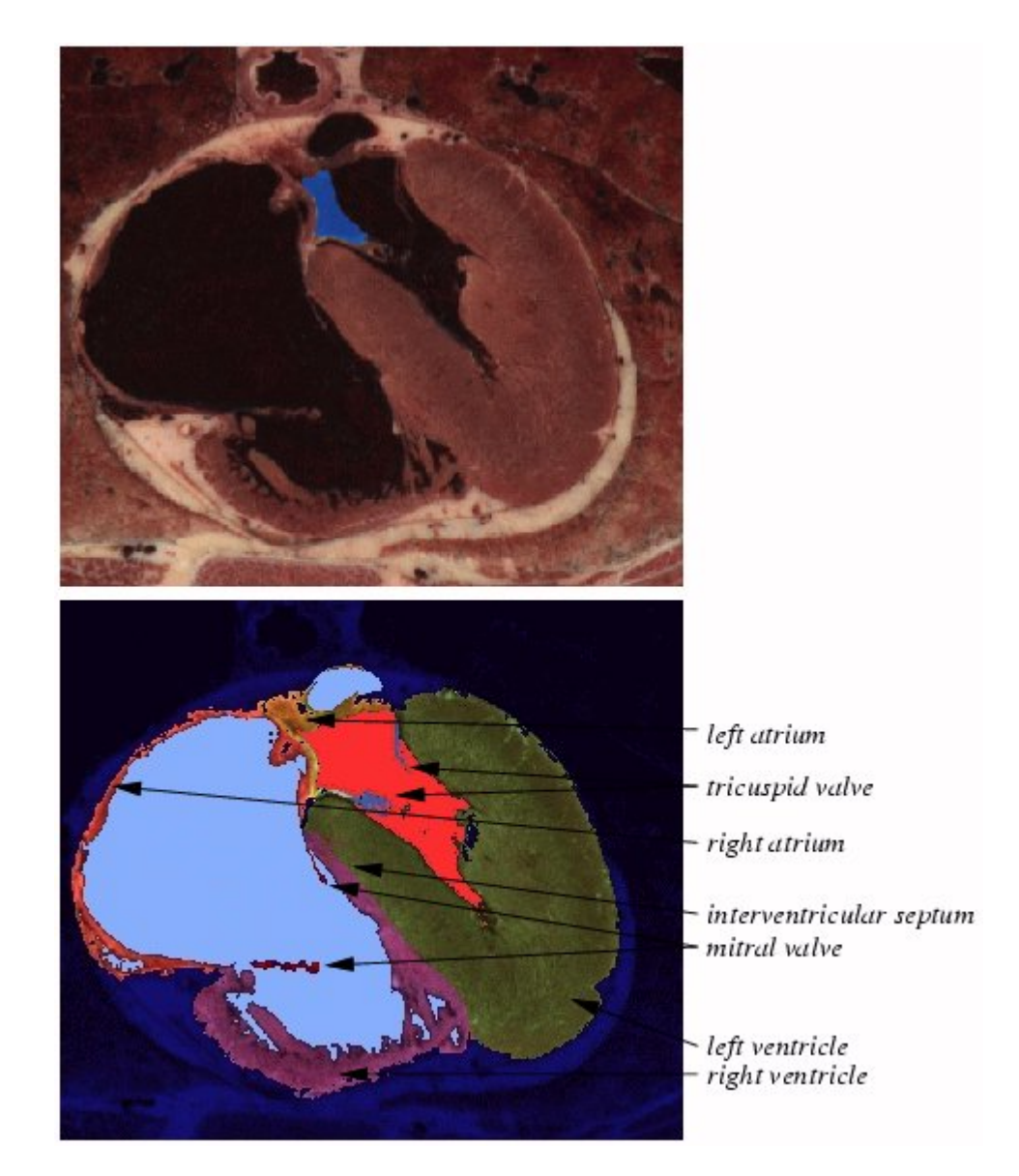


Figure 1. The upper figure shows the cross section of a human heart. The lower figure shows the same cross section with different tissue types color-coded: the dark blue blended part of the image is the tissue surrounding the heart, eg. fat, lungs. The light blue part describes the blood lacking oxygen inside the right atrium and ventricle. The bright red region is the oxygenated blood in the left atrium and ventricle. The left ventricular myocardium is blended green, the right ventricle in a violet color. The orange colored muscle structures belong to the right atrium, the left atrium is blended in a yellow/brown color. In addition, the mitral and tricuspid valve are shown separating the atria from the ventricles.

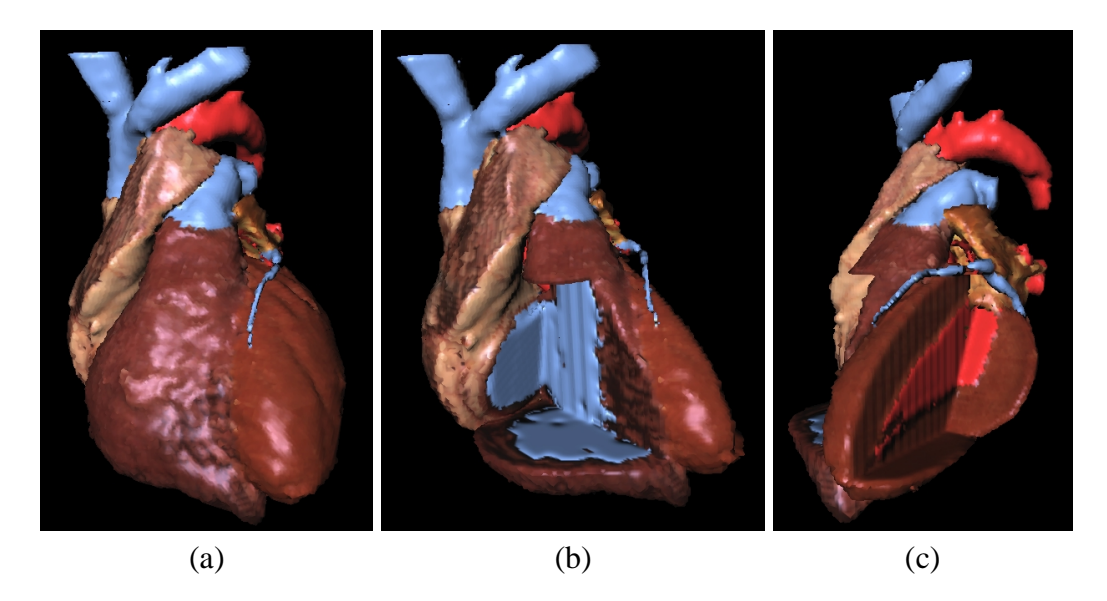


Figure 2. Different views of the anatomy of a human heart: Figure (a) shows a ventral view of the heart; the blood, the atria and ventricles are color-coded with regard to the type of tissue. (b) The right ventricular wall is cut. Therefore a view of the interventricular septum is enabled. Figure (c) shows a view onto the interventricular septum due to the absence of the left ventricular wall.

The myocardial tissue is composed of myocytes and therefore able to contract and supply mechanical power to pump blood into the body. As skeletal muscle, the myocardial tissue shows anisotropic behavior regarding mechanical properties as well as electrical properties. Additionally, the heart contains the specialized electrical conduction system. It consists of different fibers showing different histological properties. The sino-atrial node (SA-node) is located at the border between the right atrium and the vena cava superior, more at the outside of the heart. Another fiber structure of the cardiac conduction system is the atrio-ventricular node (AV-node). It is part of the right atrium and located in the interatrial septum at the atrio-ventricular border. Beginning with the atrio-ventricular node (AV-node) at the border between right atrium and ventricles the electrical conduction system is structured like a tree with the AV-node as root. It continues with the bundle of His and spreads along the interventricular septum branching to the left and right bundle branches. The left bundle branch is again split into an anterior and posterior part. Finally, the Purkinje fibers are reached which are terminated at the endocardium [6].

Image Data

The anatomical models generated within this work are based on the tomographic scans and photos of the Visible Man dataset of the National Library of Medicine, Bethesda, Maryland (USA) [2][3]. The created models are part of the MEETMan Project [7][8][9][10][11] of the Institute of Biomedical Engineering, University of Karlsruhe (Germany). The image data was created applying different techniques of medical imaging to the corpse of a 39 year old, 1.80 m sized and 93 kg weighty man sentenced to death. Computed Tomography (CT) scans, Magnetic Resonance Imaging (MRI) scans and cryosections were created in different spatial resolutions. The photo data of the cryosections are of the best quality within this multi-modal dataset regarding contrast and spatial resolution. Within one photo, the size of each pixel is $1/3 \times 1/3 \times mm^2$ leading to a total of 2048×1280 pixels per photo. Each pixel is composed of 3×8 bit for the red-, green- and blue-channel of the photo. The distance between the 1878 photo layers is 1 mm. Figure 3 shows a layer of the photo and CT image data of the Visible Man dataset.

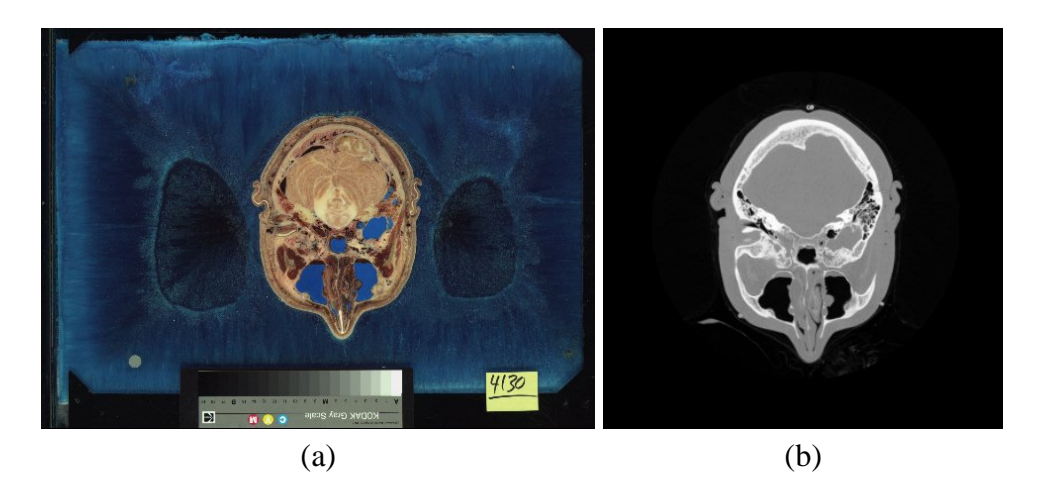


Figure 3. Visible Man raw image data, cross sections of the head: (a) shows the photo data, (b) the CT scan.

Digital Image Processing

Improving the Raw Image Data

At first, the raw image data are pre-processed to correct deficiencies in the alignment of the layers and to interpolate missing or unusable layers. The alignment correction is performed detecting a circular pattern (see the lower left part of figure 3 a) in each layer of the dataset by means of 2D image correlation techniques [12][7][13]. An interpolation algorithm is applied to those layers that are missing or of a poor image quality. This algorithm is based on a semi-interactive warping method [14]. Therefore, the user defines N pairs of points p

$$\vec{p} = \begin{pmatrix} \vec{u} \\ \vec{v} \end{pmatrix}$$
 where $\vec{u} = \begin{pmatrix} x \\ y \end{pmatrix}$ and $\vec{v} = \begin{pmatrix} x' \\ y' \end{pmatrix}$ (1)

in the layers surrounding the layers selected for interpolation. Each defined point u_i with $i=1,\ldots,N$, is called an anchor point and is defined in the layer above the unusable section (first layer) of image data. The corresponding points v_i with $i=1,\ldots,N$, are defined in the layer below the unusable section (last layer). The anchor points and its corresponding points may be anatomical landmarks, e.g. the center of a bone or any border between different types of tissue (see Figure 4).

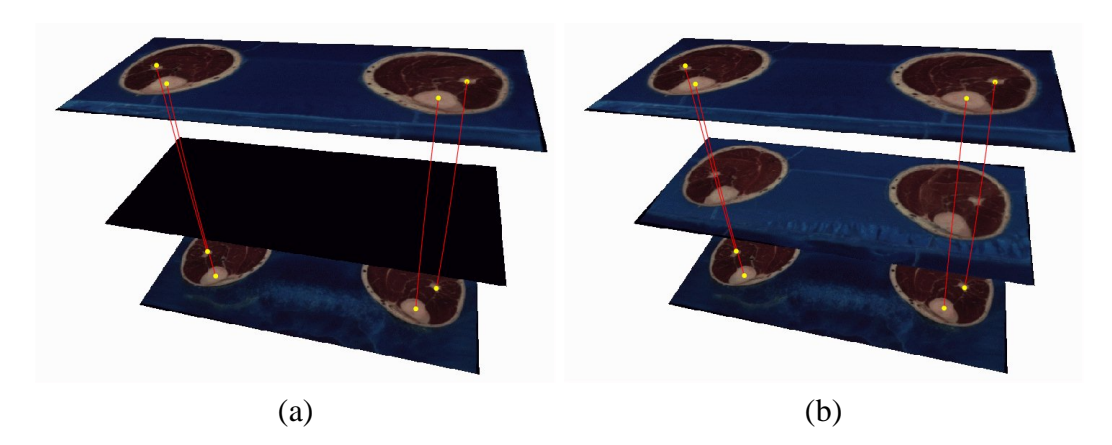


Figure 4. Interpolation of unusable layers: the anchor points are marked yellow. The red line describes the path from the anchor points in the first layer to the corresponding points in the last layer. This path is interpolated by a cubic spline. The figures show the photo data before (a) and after (b) the interpolation process.

Regarding the transformation of the anchor points to the corresponding points, it is possible to define a transformation for all points of the first layer to the last layer. By means of radial basis functions it is possible to calculate a radial basis transformation R(u) for any point u in the first layer as follows. Since R(u) is separable, it can be expressed as:

$$R(\vec{u}) = \begin{pmatrix} R_X(\vec{u}) \\ R_Y(\vec{u}) \end{pmatrix}. \tag{2}$$

 R_X and R_Y are radial functions of the form

$$R_X(\vec{u}) \, = \, \sum_{i=1}^N a_{i,x} g(|\vec{u} - \vec{u}_i|)$$

$$R_Y(\vec{u}) \, = \, \sum_{i=1}^N a_{i,y} g(|\vec{u} - \vec{u}_i|).$$

The radial basis function g is a decreasing function. Several functions exist suitable as radial basis function. For example, the Gaussian function

$$g_{\sigma}(t) = e^{-t^2/\sigma^2} \tag{3}$$

is used while interpolating the unusable layers. The influence of the transformation R on an arbitrary point u depends on the distance of u to the anchor points u_i . With increasing distance, the influence of the transformation on u declines due to the decreasing value of $g(|u - u_i|)$. To calculate the parameters $a_{i,x}$ and $a_{i,y}$ of the transformation matrix R for a given set of N anchor points u_i , i = 1, ..., N and a given radial basis function g it is necessary to solve the following system of equations:

$$R_X(\vec{u_i}) = \sum_{j=1}^{N} a_{j,x} g(|\vec{u_i} - \vec{u_j}|) = x_i' - x_i$$

$$R_Y(\vec{u_i}) = \sum_{j=1}^{N} a_{j,y} g(|\vec{u_i} - \vec{u_j}|) = y_i' - y_i$$
for $i = 1, \dots, N$. (4)

Once the transformation R is defined, all points of the first layer are transformed to replace the unusable image data. Figure 4 shows some results of the interpolation.

Segmentation and Classification

To create an anatomical model of the body, the Visible Man image data are segmented and classified into approximately 40 different tissue classes. Therefore different segmentation techniques are applied to the pre-processed image data. Large parts of the data are segmented using a 3D region growing [13] technique (see figure 5) working on multi-modal data [8].

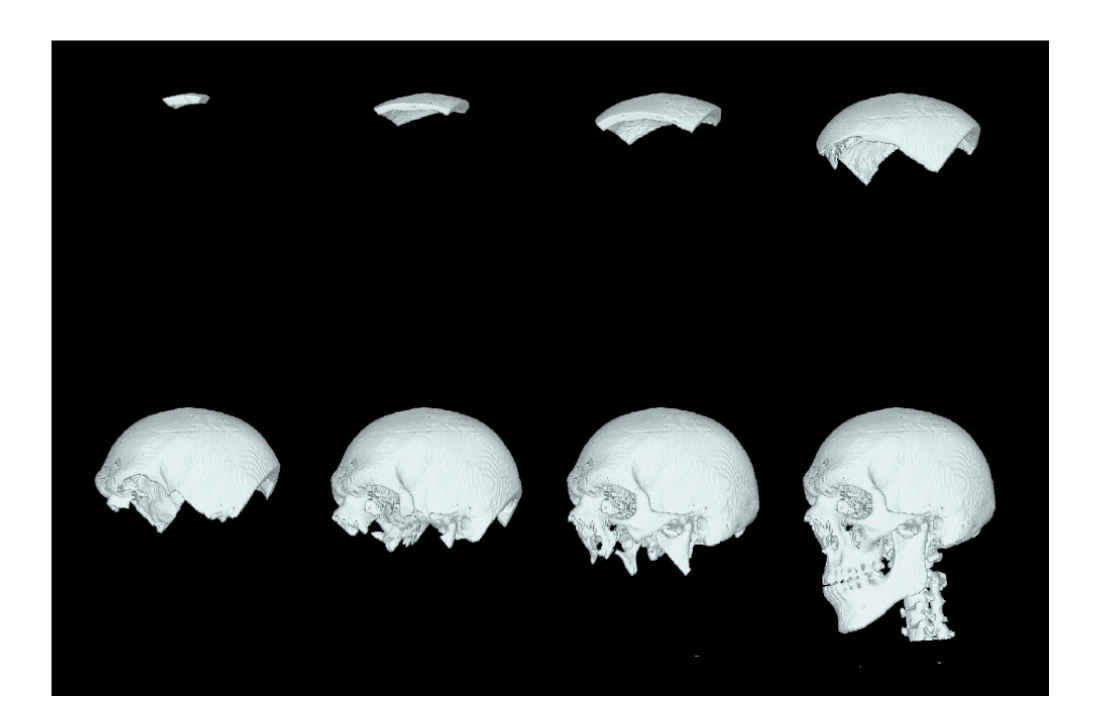


Figure 5. 3D region growing: the seed point is set next to the top of the skull. The region grows until the skull is segmented.

Applying the region growing technique to the image data, the user selects one or more initial seed points as start point for the region growing process. The region growing algorithm checks, whether the neighboring points of the seed points belong to the same segment as the seed points by evaluating the color (or gray) values of the neighboring points. If they belong to the same segment, these points are taken as seed points in the next step and the region growing algorithm continues with checking the neighbors of the new seed points. This is done iteratively until no new seed points can be found. To avoid an incorrect classification, the segmentation is supported by inserting surfaces interactively at areas of bad image contrast between neighboring types of tissue. The classification is done implicitly when segmenting the image data. As result of this segmentation and classification a dataset of the human anatomy is created. This anatomical model is shown in Figure 6

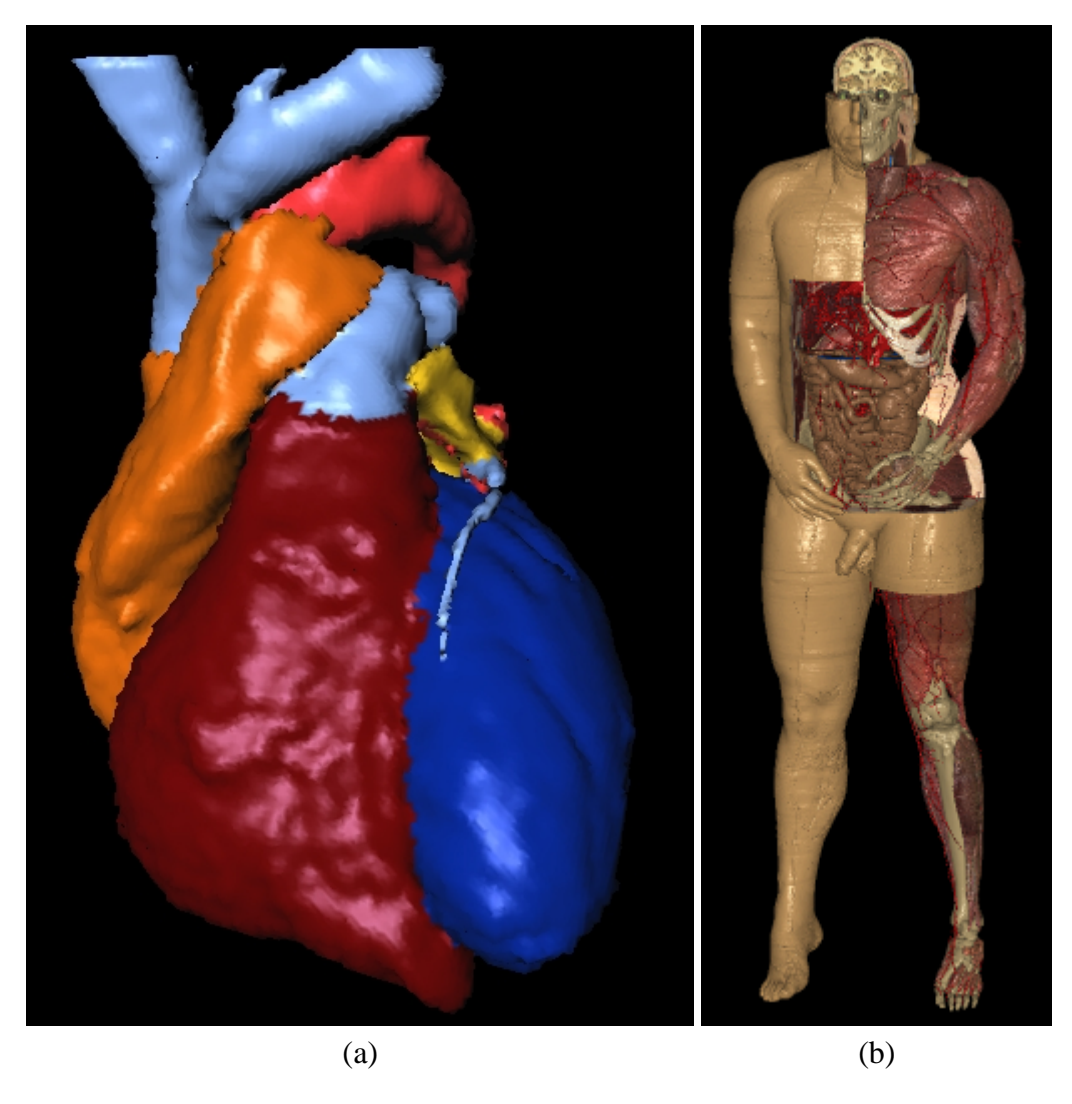


Figure 6. Anatomical models of the human body: Figure (a) shows a ventral view of the heart. The different tissue classes left atrium, right atrium, left ventricle, right ventricle, arterial and venous blood are visualized with different colors assigned to each tissue class. Figure (b) shows the anatomical model of the entire body.

Muscle Fiber Orientation

The cardiac muscle shows anisotropic behavior regarding mechanical properties as well as electrical properties. Thus, to simulate the electrical excitation propagation in the heart it is necessary to include the myocardial fiber orientation into the anatomical model of the heart. As cardiac muscle, skeletal muscle shows anisotropic behavior too. Calculating the Body Surface Potential Maps (BSPM, see section 2.2.4) the knowledge of the fiber orientation of the skeletal muscles is needed as well. Therefore, the myocardial and skeletal fiber orientation is calculated based on the Visible Man photo data and thus, the anatomical model is extended. The calculation of the fiber orientations is divided into two parts. The first part deals with the detection of fiber orientation for a set of anchor points based on texture analysis of the Visible Man photo data. The second part is based on the interpolation of these anchor points using an iterative numerical technique [9][15]. Within the initially preprocessed photo data the main axes are determined in a section surrounding the voxel chosen for automatic orientation determination by applying the Hotelling transform [13]. These automatically generated orientations are validated and as required corrected using an interactive 3D editor. Finally, the orientation of all cardiac voxels are determined by interpolation using the initially semi-automatically generated orientations as anchor points. At the start of the interpolation all voxels but the anchor points are set to the value of its' nearest neighbor. Afterwards the interpolation starts averaging in the 6-neighborhood. The

interpolation continues until the deviation of the orientations between two sequential interpolation steps falls below a minimum value. Figure 7 shows the result of this interpolation applied to the Visible Man data set.

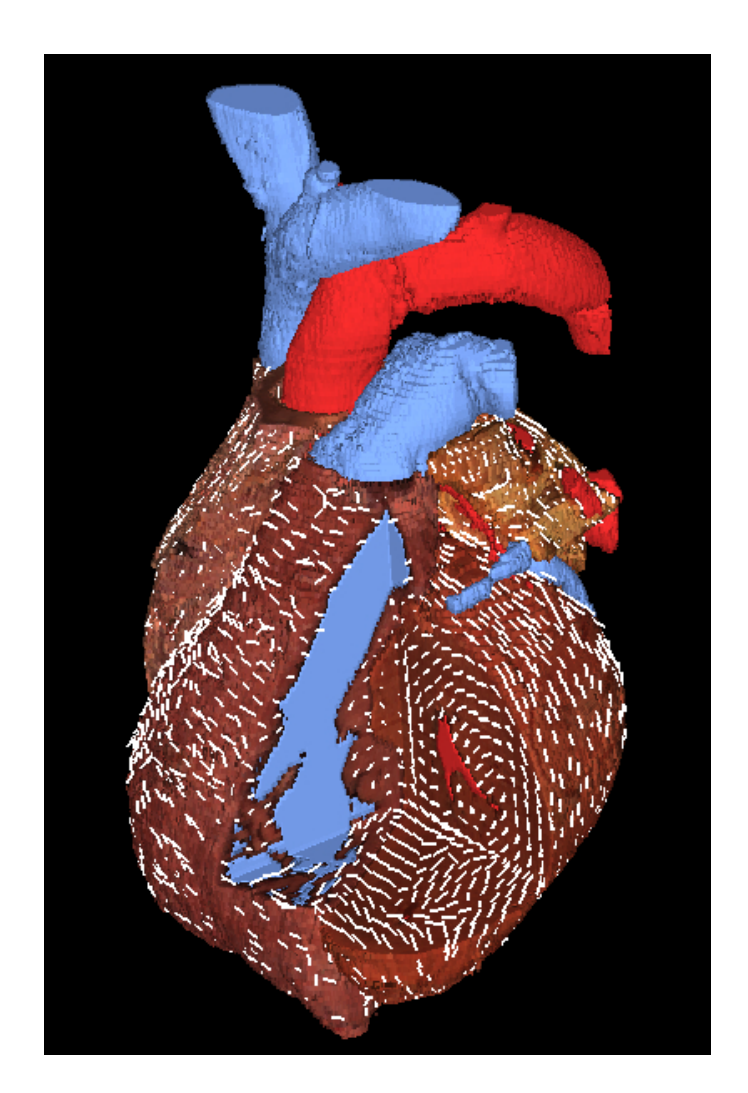


Figure 7. Heart of the Visible Man: The short white lines demonstrate the cardiac fiber orientation for each voxel.

Specialized Cardiac Conduction System

To simulate the electrical excitation propagation in the entire heart it is necessary to classify the specialized cardiac conduction system as well. Due to the limitations of the image data regarding resolution and contrast it seems to be almost impossible to create the conduction system automatically by means of digital image processing. Methods for an interactive design of the conduction system are proposed in the literature [44]. In this work the conduction system is created semi-automatically. It is represented by a tree composed of nodes and edges. The nodes are interconnected by the edges representing the spatial course of the conduction system. The root of this tree is located at the atrio-ventricular node and the leaves at the junctions of the Purkinje fibers to the ventricular myocardium. The creation of this tree is divided into three steps:

- 1. Three undirected graphs $G_i = (N_i, E_i)$ with $i = 1 \dots , 3$ are created. The set E_i contains all edges interconnecting each node of the set N_i with another node of N_i . The spatial location of the nodes of N_i are created either manually or automatically.
- 2. Three trees $S_i \subset G_i$, i = 1 ..., 3 are found that interconnect the atrio-ventricular node

with the endings of left and right bundle branches (tree S_1), the endings of the left bundle branches with the Purkinje fiber endings of the left ventricle (tree S_2) and the endings of the right bundle branches with the Purkinje fiber endings of the right ventricle (tree S_3).

3. The three trees S_i are merged to one tree T representing the specialized cardiac conduction system.

The locations of the Purkinje fiber endings, i.e. the nodes in the trees S_2 and S_3 , are generated automatically at the endocardium according to the literature [16][17][6], while the locations of the atrio-ventricular node and the left and right bundle branches nodes are created interactively by the user. The procedure of creating the edges between the nodes is referred to the problem of finding the shortest sub-spanning tree in a graph G [18][19]. Such a tree can be described by the predecessors $\pi[n]$ of each node n. The only node of the tree without predecessor is the root node. In this work an algorithm similar to Prim's algorithm [18] is implemented as follows:

1	$Q \leftarrow N[G]$	Initialize the priority queue Q to contain all nodes $N[G]$ of graph $G(N, E)$.
2	$W \leftarrow E[G]$	Initialize the weights $W[E]$ for all edges E .
3	for each $e \in E$	For each edge e of E .
4	do $W[e] \leftarrow \text{CALC-WEIGHT}(e)$	Calculate the weight $W[e]$.
5	$r \leftarrow \text{Extract-Root}(Q)$	Extract the tree's root r of Q .
6	while $Q eq 0$	While the queue Q is not empty.
7	do $e_l \leftarrow \text{Light-Edge}\left(\left(N - Q, Q\right)\right)$	Determine the light edge e_l crossing the cut $(N - Q, Q)$ according to the weights $W[E]$ of the edges E .
8	$(u, v) \leftarrow e_l$	Determine the nodes $u \in Q$ and $v \in (N - Q)$ of edge e_l .
9	$\pi[u] \leftarrow v$	Set the predecessor of node u to v .
10	$Q \leftarrow \textit{EXTRACT-NODE}(u, Q)$	Extract u from queue Q .

The weights W have a high impact on the resulting tree. In this work the weight of each edge depends on the length of the edge and the types of tissue the edge crosses by connecting two nodes. It is calculated for each edge as depicted in lines 3 to 4. The tree grows by adding the light edge e_l crossing the cut (N - Q, Q) (lines 6 to 10). The cut divides the nodes N in two parts, the part of the nodes already belonging to the tree and the part of nodes still not connected to the tree. An edge connecting two nodes, where one node belongs two the tree and the other not, crosses the cut. The light edge crossing the cut is the edge with the smallest weight. It is guaranteed to find the smallest subspanning tree by adding the light edge to a tree each time the tree grows. Figure 8 shows the semi-automatically created specialized ventricular conduction system. It is composed of the atrio-ventricular node as root, the bundle of His, the left and right bundle branches and the Purkinje fibers.

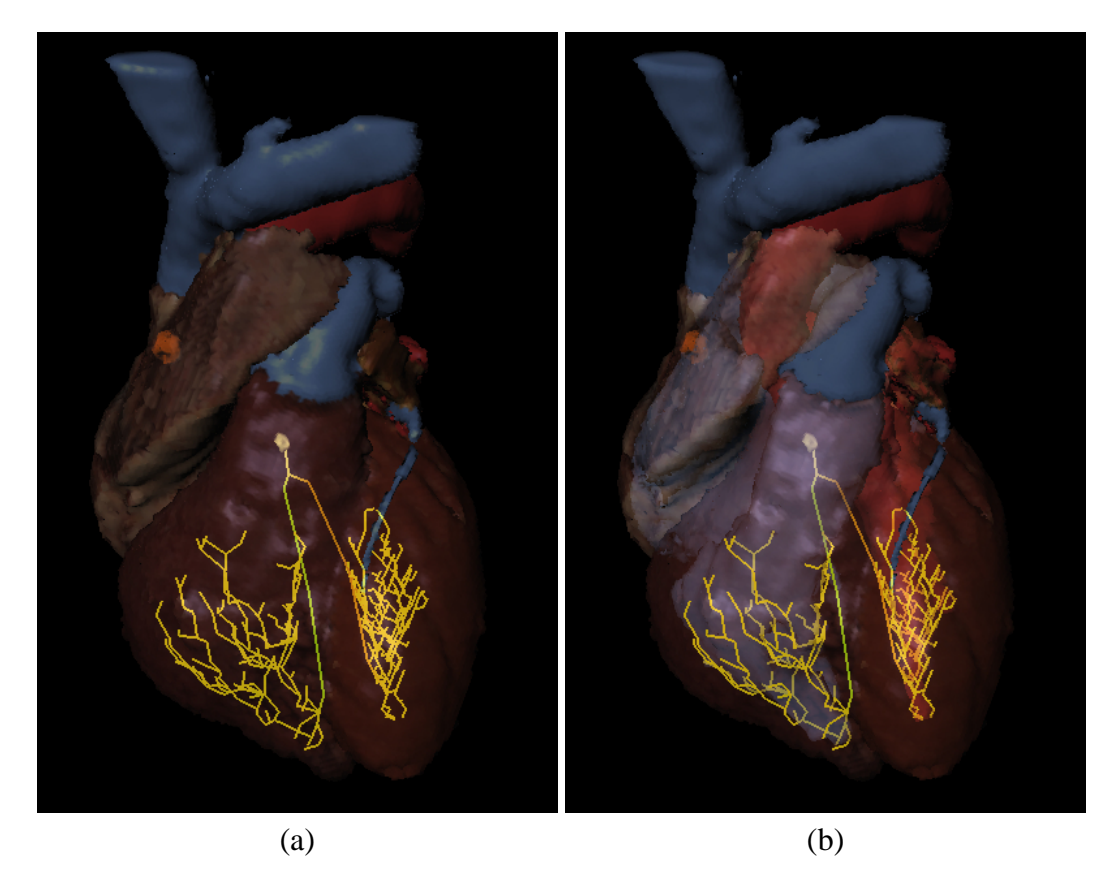


Figure 8. Specialized cardiac conduction system modeled as tree: the yellow lines show the locations of the fibers in anatomical context. In figures (a) and (b) the surface of the myocardium is visualized semi-transparent. The atrio-ventricular node is the root of the ventricular conduction system. It is located at the boundary between ventricular and atrial myocardium. The conduction system fans out, beginning with the bundle of His, continuing with the left and right bundle branches and finally ending with the Purkinje fibers. The sino-atrial node is visualized in the right atrium although it is not part of the ventricular conduction system. In addition, in figure (b) the arterial and venous blood is displayed to demonstrate the location of the Purkinje fiber endings close to the endocardium.

Modeling the Cardiac Electrophysiology

Human Cardiac Electrophysiology

To provide the cells of the body with oxygenated blood, the heart pumps blood periodically through the vessels into the body by contracting the cardiac muscles. This contraction is coupled to the electrical excitation propagation in the human heart. Therefore, the physiological temporal and spatial course of this excitation is of prime importance for the correct function of the heart. Due to differences between ion concentrations inside and outside a cardiac cell, a potential difference rises across the cell membrane [20]. This transmembrane potential varies depending on various parameters. The resting potential (approximately around - $90 \, mV$) is reached at equilibrium, a state where the absolute values of chemical and electrical gradients are equal but the directions of these gradients are opposite [20]. If a cell is excited the transmembrane potential rises. Then the cell is depolarized. An excited cell may propagate its excitation to its neighboring cell depending on the tissue characteristics and the transmembrane potentials of its neighboring cells as well as on the interconnections between the cell and its neighbors [21]. On successful propagation, the transmembrane potential of the neighboring cells is altered according to its' tissue characteristics and ion concentrations. Taking the tissue characteristics of each cell into account an excitation may propagate all over the myocardium starting at a small group of cells. To ensure a physiological mechanical contraction and therefore a correct pump mechanism of the heart, the electrical excitation propagates over a large area of the heart along the specialized cardiac conduction system. In a healthy human heart pacemaker cells take control over the initiation of an excitation, which is spread throughout the heart. Usually the excitation starts in the sino-atrial node (SA-node) spreading all over the atria. The excitation reaches the atrio-ventricular node (AV-node), where it is delayed according to the AV-nodes' tissue characteristics. The ventricles are not excited from the atrial myocardium since there is no direct electrical connection from atrial myocardium to ventricular myocardium. From the AV-node the excitation propagates along the bundle of His, the left and right bundle branches and finally reaches the Purkinje fibers. Reaching the endings of the Purkinje fibers the excitation is spread over the left and right ventricles [22][5][6]. On failure of the sino-atrial node the secondary pacemaker cells of the AV-node take control over the initiation of the excitation to protect the heart and therefore the entire body from total collapse. The Purkinje fibers itself may also initiate the excitation if the AV-node fails [22].

Simulation using a Cellular Automaton

Cellular Models

Numerous models of cardiac cellular electrophysiology exist computing the transmembrane potential, currents, ion concentrations and other parameters of a cardiac cell for a specific type of tissue [23][24][25]. Usually, these models contain a set of coupled differential equations. The number of these differential equations has been increasing within the last years and meanwhile reached 50 differential equations [26]. To solve these differential equations numerically a lot of computational power and time is needed considering a simulation not only of a single cell but in the entire heart. Therefore, this work focuses on a simulation using a cellular automaton. The excitation of cells propagates according to rules generated from cardiac electrophysiology. No differential equations are solved here, the computational velocity for one cardiac cycle on a detailed anatomical model of the heart is much higher.

Cellular Automaton

Cellular automata are used in various fields as models of natural processes e.g. in physics, chemistry, biology, economy and medicine [27][28][29][30][31][32][33]. A cellular automaton can be divided in two components [34]:

- 1. A regular, discrete, infinite network represents the architecture, the universe or the underlying space structure.
- 2. At each node of the network a finite automaton [35] is working.

A node of the network is called a cell. Each cell corresponds with a finite set of other cells. The number of cells one cell communicates with determines the neighborhood of the cellular automaton. The way two cells communicate is local, deterministic, uniform and synchronous. Therefore, a global evolution of the system is predetermined running the cellular automaton along discrete time steps [34]. The number of cells a cell communicates with defines the neighborhood of the cellular automaton. Classical neighborhoods are the nearest neighbors neighborhoods of von Neumann or Moore. In case of 3-dimensional cellular automatons these are the 6- respectively 26-neighborhood. The set N usually is an ordered subset of Z representing the neighbors of a cell. Usually N is fixed and does not vary dependent on the cell. In this work a 3-dimensional cellular automaton (\square) B = (\mathbb{Z}^3 , S, N, δ) is used to simulate the propagation of electrical excitation of one cardiac cell to their neighbors. Unlike classical cellular automata, the neighborhood N varies dependent on each cell in this work. The underlying space structure is defined by the anatomical model of the heart. This model consists of the classified anatomical tissue data set derived from the Visible Man data, the muscle fiber orientation data set and the specialized cardiac conduction system tree. While the muscle fiber orientation data set has only an impact on the local transition function $\delta: S^{n+1} \to S$, the conduction system tree varies the neighborhood of the cells located at the nodes of the tree. For these cells the 26 fixed neighbors are extended by the set of successors and one predecessor of the tree. However, most of the cells have a fixed set N_{fixed} of 26 neighbors, whereas only for a very small number of the cells (approx. 0.01 %) the neighborhood N varies. Figure 9 shows an exemplary neighborhood configuration.

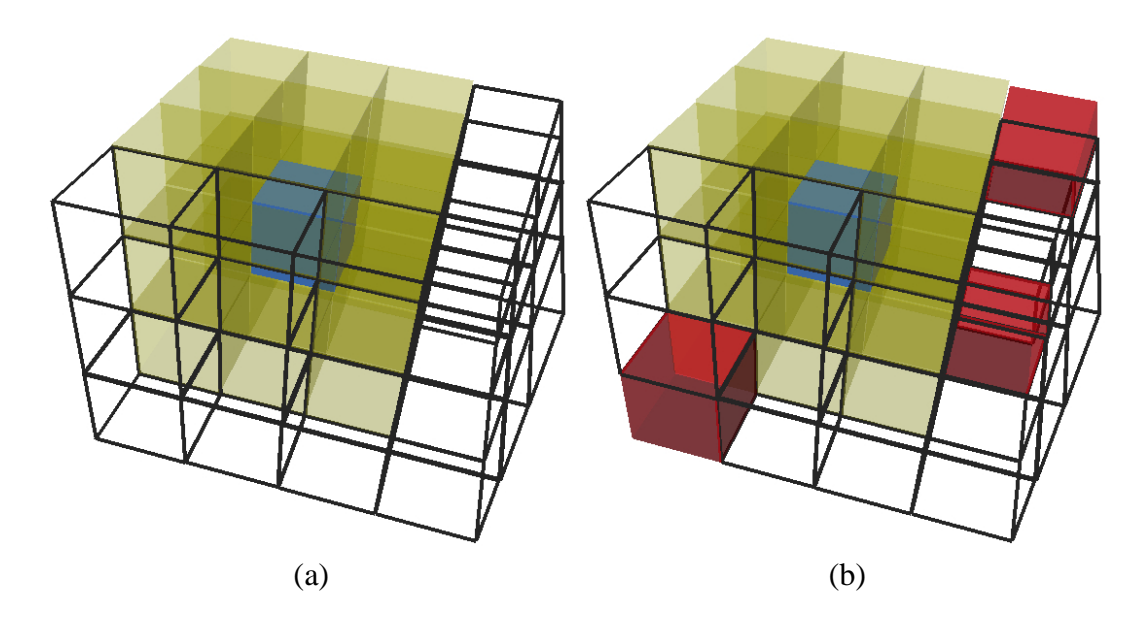


Figure 9. Figure (a) depicts a classical 26-neighborhood (Moore) of a cellular automaton. The yellow cells are the neighbors of the blue cell. Figure (b) shows the extension of the 26-neighborhood of figure (a) with cells of the cardiac conduction system tree (marked red). For this case the neighborhood is a 29-neighborhood.

The excitation propagation is simulated by passing action impulses from one cell to its neighbor under certain conditions. These conditions are summarized under the rule $\delta: S^{n+1} \to S$ of the cellular automaton. It alters the state of a cell according to its state and the state of its n neighbors. The rule incorporates knowledge of electro-physiological parameters dependent on the type of cardiac tissue e.g. the refractory time, autorhythmicity and the anisotropic conduction velocity. Figure 10 depicts the finite automaton which changes the state of a cell.

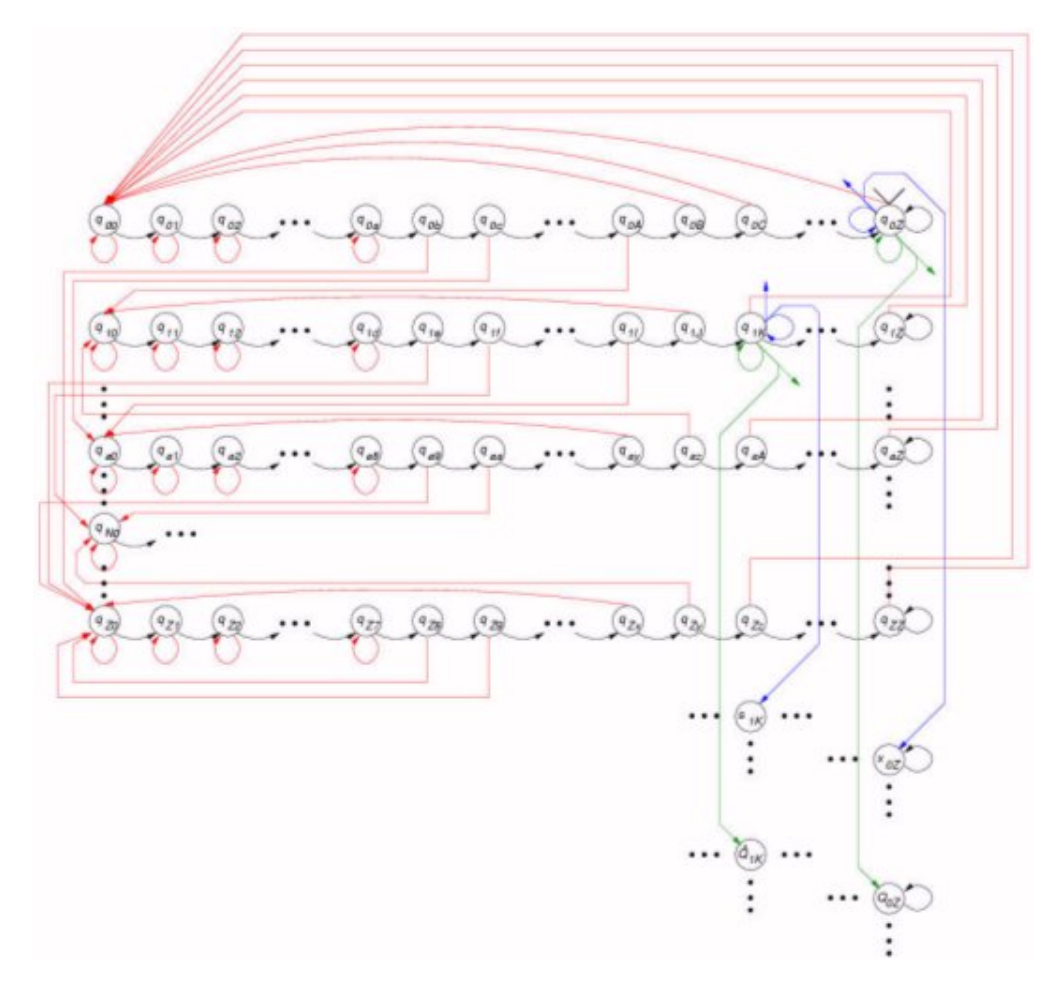


Figure 10. Partial state diagram of the finite automaton working on each cell of the cellular automaton: The alphabet Σ of the automaton contains four elements displayed as differently colored arcs, $\Sigma = \{black, red, green, blue\}$. "black" depicts the increment of time while running the cellular automaton, "red" a stimulus generated due to excitation propagation, autorhythmicity or external interaction. "green" describes the alternation of the tissue class and therefore the change of the electro-physiological tissue characteristics. Any change of fiber orientation results in a "blue" input event.

The result of a simulation using this cellular automaton \mathfrak{B} is the temporal and spatial distribution of the transmembrane potential for each cell of the cellular automaton. This distribution allows further numerical calculations of physical fields in the human body, e.g. the current source distribution in the heart and the extracellular potentials in the whole body.

Electrical Sources

Bidomain Model

Due to the big amount of cardiac cells in the heart a simulation on a cellular level seems to be impossible for the entire heart on a common workstation. A possibility to calculate currents on a rather macroscopic point of view offers the bidomain model [36][37]. It averages the discrete structure of cardiac tissue combining extracellular and intracellular space to two continua of identical location separated by the cell membrane. At each point of these continua the electrical properties of intracellular and extracellular space and the membrane are defined and can be described by the following equations [36]: The intracellular and extracellular current densities J_i and J_o can be calculated by the product of the gradient of the intracellular and extracellular potential Φ_i and Φ_o with their effective conductivities $\vec{\sigma}_i$ and $\vec{\sigma}_o$ respectively. The effective conductivities are defined by the

specific conductivities weighted with their volume fraction.

$$\vec{J_i} = -\vec{\vec{\sigma}_i} \nabla \Phi_i \tag{5}$$

$$\vec{J_o} = -\vec{\bar{\sigma}_o} \nabla \Phi_o \tag{6}$$

$$\vec{J} = \vec{J_i} + \vec{J_o}$$

$$= -\vec{\vec{\sigma}}_i \nabla \Phi_i - \vec{\vec{\sigma}}_o \nabla \Phi_o \tag{7}$$

Using the definition of the transmembrane potential

$$\Phi_m = \Phi_i - \Phi_o \tag{8}$$

the total current density \bar{J} from (7) can be written as

$$\vec{J} = -\vec{\vec{\sigma}}_i \nabla \Phi_m - \left(\vec{\vec{\sigma}}_o + \vec{\vec{\sigma}}_i\right) \nabla \Phi_o \tag{9}$$

and with $\nabla \vec{J} = 0$

$$\nabla \left(\vec{\sigma}_i \nabla \Phi_m \right) = -\nabla \left(\vec{\sigma}_H \nabla \Phi_o \right) \quad . \tag{10}$$

The conductivity $ec{m{\sigma}}_{m{H}}$ is the sum of the effective conductivities of the intracellular and

extracellular space. The left side of equation (10) denotes the strength of the impressed current density which arises from the spatial gradient of the transmembrane potential:

$$I_m = \nabla \vec{J}^i = -\nabla \left(\vec{\vec{\sigma}}_i \nabla \Phi_m \right) \tag{11}$$

Body Surface Potential Map

To simulate standard ECG leads or Body Surface Potential Maps (BSPM) it is necessary to calculate the potential distribution V in the body. Therefore, the generalized Poisson equation (eq. 12) must be solved:

$$\nabla \left(\vec{\sigma} \nabla V \right) = I_m \quad . \tag{12}$$

The conductivity distribution $\vec{\sigma}$ in the body must be given as well as the source current distribution I_m in the heart. A volume conductor model of the human body based on the anatomical model of the Visible Man body (MEETMan) is used as conductivity distribution regarding the anisotropic tissue properties of skeletal and cardiac muscle. The source current distribution is generated applying the bidomain equations to the transmembrane potential distribution generated by the cellular automaton. The Poisson equation is solved numerically by means of the finite difference method. The applied solver is based on the Full-Multigrid-Algorithm [38][39][9][40]. Once the potential V is calculated, the BSPM can be created displaying the potential distribution on the body surface. In addition, placing virtual

electrodes on the body surface it is possible to calculate the ECG leads and compare these to values in the literature [22][41].

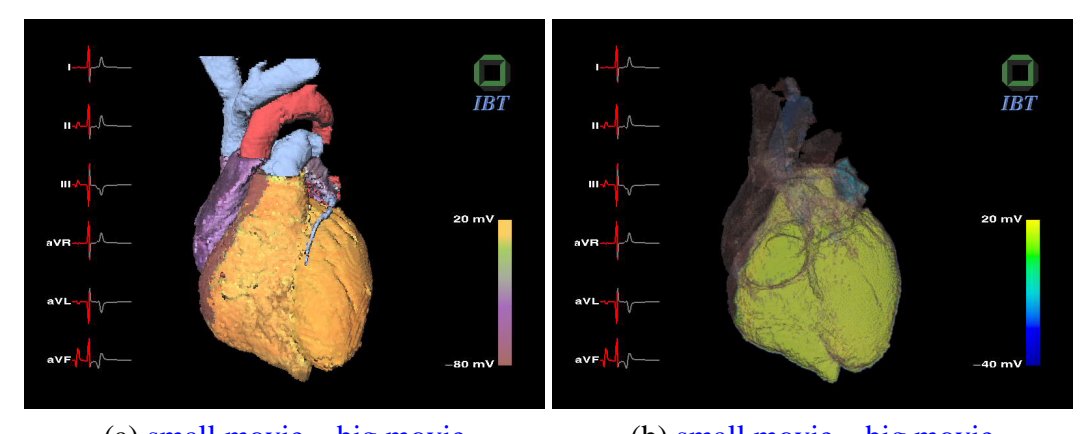
Results

Overview

Different simulations of the electrical excitation propagation in the human heart are performed. They are based on anatomical models of the human heart and body generated as described in section Digital Image Processing. The models consist of cubic voxels each assigning a tissue class to the underlying spatial domain. In addition, the fiber orientation of cardiac and skeletal muscle voxel is provided by the anatomical models. Finally, the specialized cardiac conduction system modeled as a tree structure extents the anatomical model. The cubic voxels of the heart model are sized 1 mm (edge length), whereas the edge length of one voxel of the used body model is 3 mm. The electrical excitation propagation is simulated by means of a cellular automaton. Different electro-physiological characteristics of the diverse tissue classes of the heart are taken into account as well as the anisotropic behavior regarding the excitation velocity. The temporal and spatial transmembrane potential distribution is calculated. These results are visualized applying advanced techniques of computer graphics [42]. In addition to the transmembrane potential distribution, the source current distribution is calculated and visualized. These current distributions are taken to calculate the potential distribution in the body by solving the generalized Poisson equation (eq. 12). Body Surface Potential Maps are derived from this potential distribution. Finally, standard ECG leads are derived and visualized. In addition to the sinus rhythm different pathologies are simulated by changing the anatomical or electro-physiological parameters of the models. These pathologies include a right bundle branch block, the WPW syndrome and the simulation of an infarction.

Sinus Rhythm

A healthy heart usually beats at sinus rhythm. The excitation starts at the SA-node, spreads over the atria reaching the AV-node. From there, the excitation is propagated along the cardiac conduction system until the Purkinje fiber endings are reached which are connected to the ventricular myocytes. Finally, the excitation is spread over the ventricles. Simulations results are displayed in Figure 11 and are animated by clicking on the images.



(a) small movie big movie

(b) small movie big movie

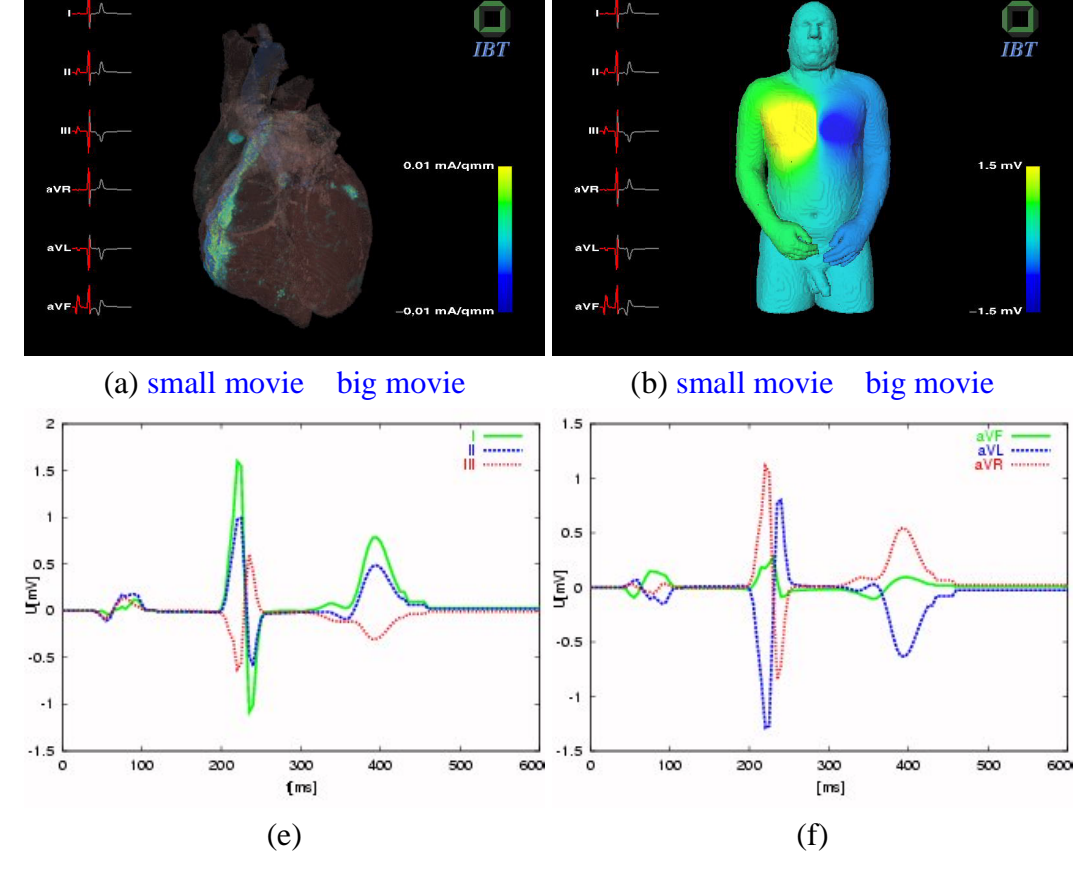
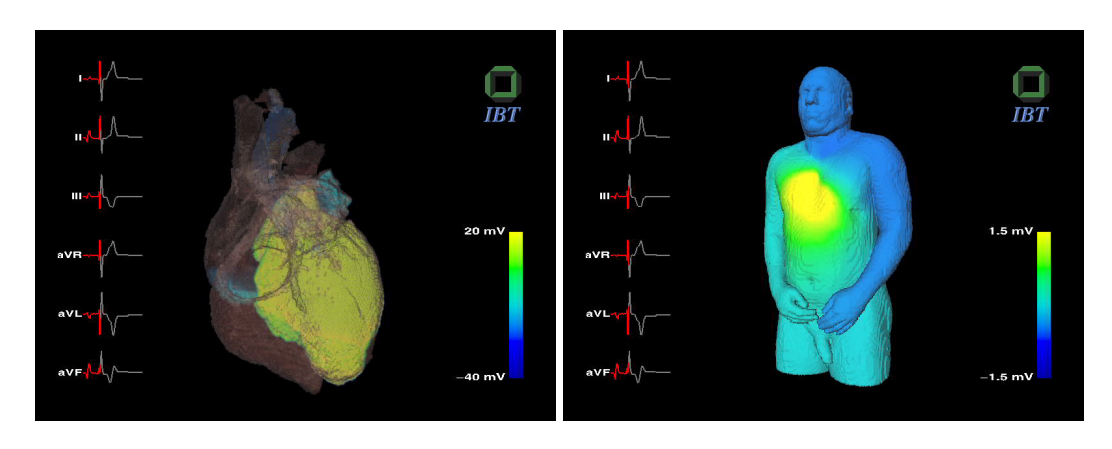


Figure 11. Simulation of sinus rhythm: The images show the transmembrane potential distribution (a,b), the source current density (c), the Body Surface Potential Map (d) for one simulation step and the ECG leads of Einthoven (e) and Goldberger (f). Two visualization techniques are used in the figures (a-d) to display the physical field distributions: In figures (a) and (d) the fields are shown on the surface of the heart respectively body. In figures (b-c) a volume visualization technique is used to display the transmembrane potential (b) and source current density (c). The different field distribution are displayed color coded according to the scale in each image.

Right Bundle Branch Block

A right bundle branch block is simulated by interrupting the specialized cardiac conduction system in the right bundle branch. Thus, the excitation propagation stops at the right bundle branch, whereas it is spread along the left part of the conduction system. Reaching the Purkinje fiber endings of the left ventricles the excitation propagates over the entire ventricular myocardium. The right ventricle is depolarized delayed due to the block in the left bundle branch (see Figure 3.3).



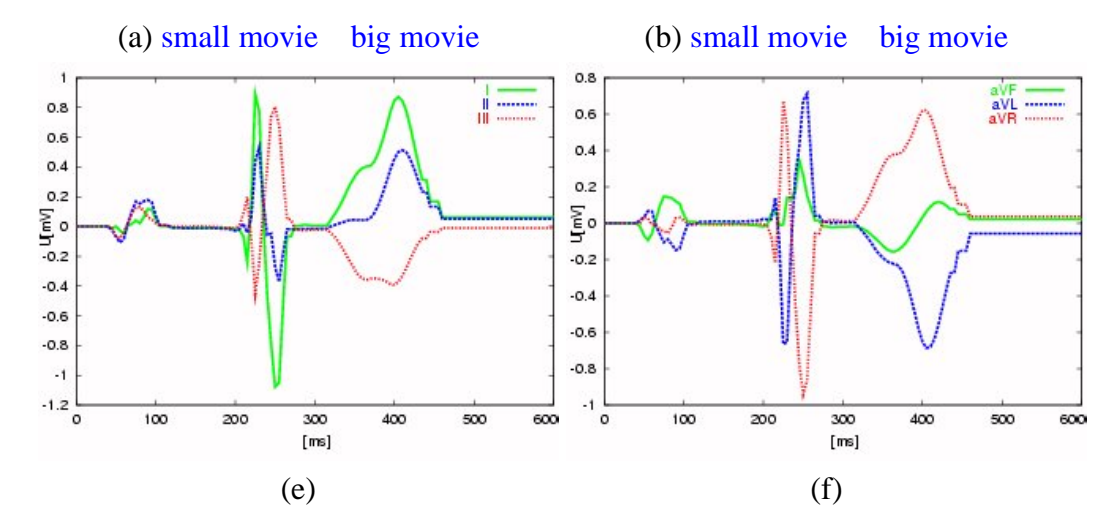


Figure 12. Simulation of a right bundle branch block: The excitation is delayed at the right ventricle. Figure (a) shows the transmembrane potential distribution, figure (b) the Body Surface Potential Map. The Einthoven and Goldberger ECGs are displayed in figures (c) and (d).

Wolff-Parkinson-White Syndrome

The Wolff-Parkinson-White (WPW) syndrome is simulated by establishing an additional electrical path from the atria to the ventricles next to the AV-node. This path bypasses the AV-node with a higher excitation velocity, resulting in a reduced *PQ*-interval in the ECG and a faster excitation propagation in the ventricles. The results of the simulations are displayed in Figure 3.4.

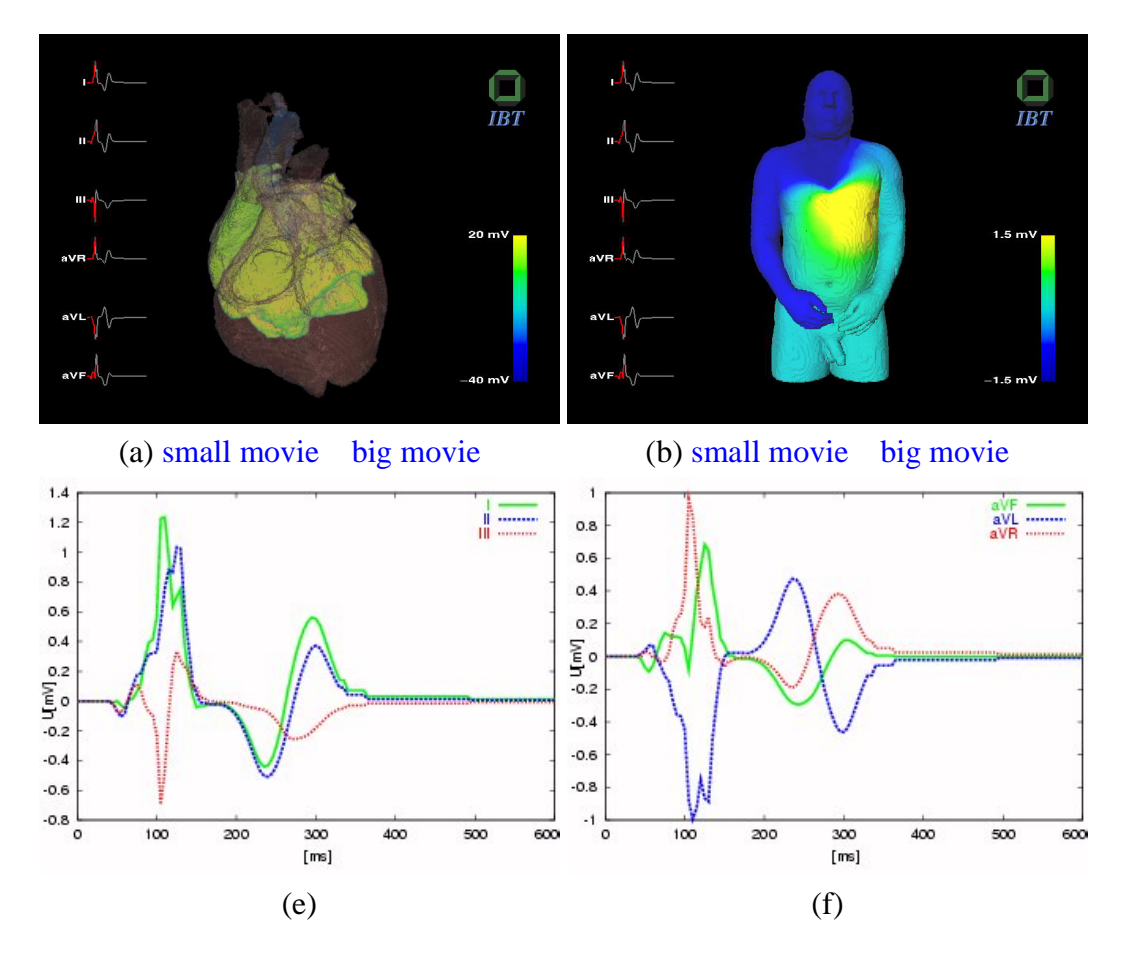


Figure 13. Simulation of a WPW syndrome: The excitation bypasses the atrio-ventricular node and spreads directly onto the ventricles (a). Figure (b) shows the Body Surface

Infarction

A transmural infarction in the left ventricular free wall is simulated defining three additional tissue classes for ischemic, injured and necrotic myocardium. The tissue characteristics of these tissue classes are modified according to values in the literature [22]. The results are shown in figure 3.5.

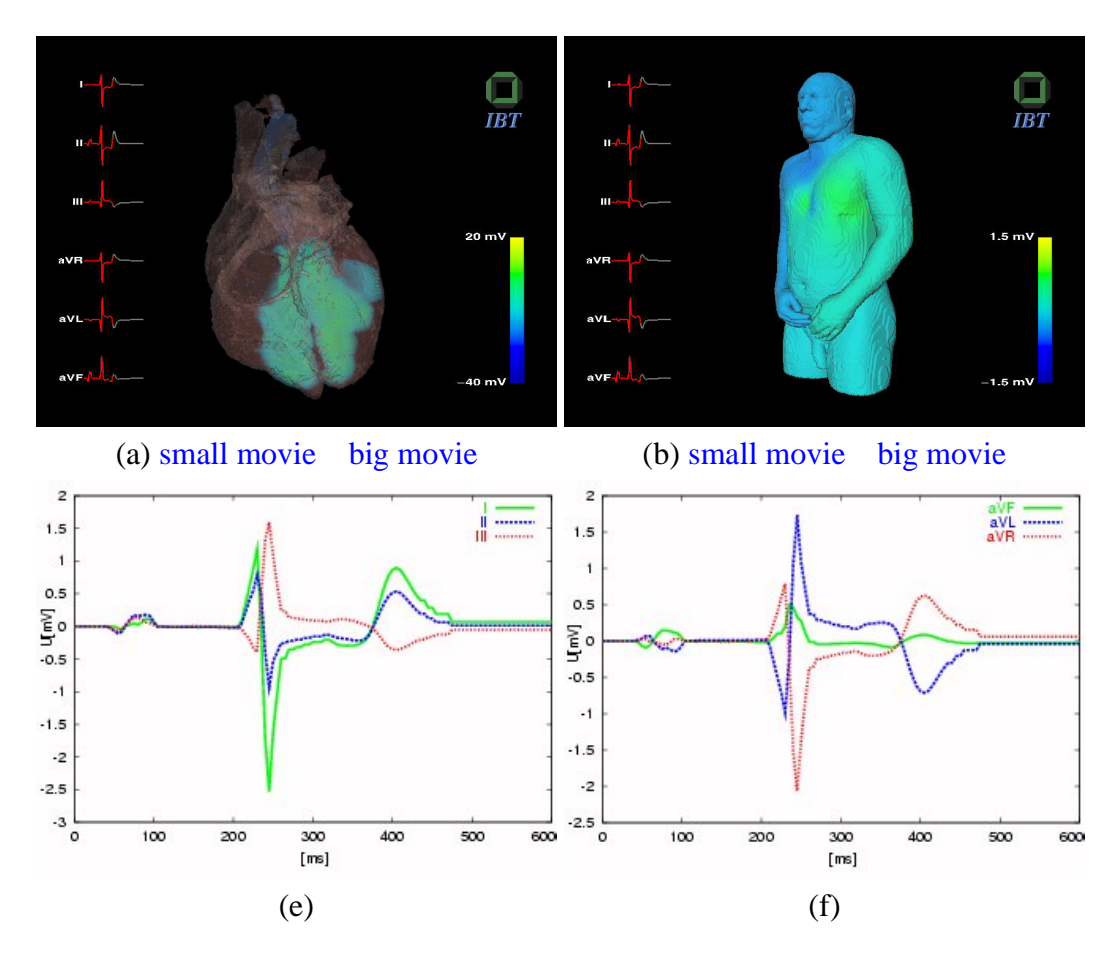


Figure 14. Simulation of a transmural infarction located at the left ventricular free wall: The excitation velocity and refractory times change in the area of the infarction. The effects on the transmembrane potential are shown in figure (a). The repolarization is delayed in the area of the infarction. This leads to a change of the potential during the repolarization phase which is displayed as color difference at the arms in figure (b). The resultant offset of the potentials during the ST interval is shown in the ECGs in figures (c) and (d).

Conclusions

In this work the simulation of the electrical excitation propagation based on tissue classified anatomical data sets is presented. Thus, methods to create these anatomical models based on digital image processing techniques applied to medical image data are outlined. These methods include techniques for segmentation of medical image data as well as techniques to determine the muscle fiber orientations. In addition a technique to create the specialized cardiac conduction system semi-automatically is described. Based on these models, simulations of the sinus rhythm as well as of different kinds of pathologies are conducted and compared to literature values. These simulations are performed by means of a cellular

automaton including anisotropic tissue properties for different cardiac tissue classes. Source current densities are calculated applying the bidomain equations to the resultant transmembrane potential distribution of the cellular automaton. Finally, the Body Surface Potential Maps are calculated solving Poisson's equation using a finite difference fullmultigrid solver regarding the inhomogeneous tissue distribution as well as anisotropic properties of the muscle structures in the body. Using these Body Surface Potential Maps, standard ECGs are derived which show good conformity to values in the literature. The resultant different physical fields are visualized applying advanced techniques of computer graphics. These visualizations give new insight into the complex electro-physiological processes of the heart on a macroscopic point of view and therefore may be of interest in medical education. The simulation by means of the cellular automaton based on the anatomical model of the Visible Man heart is efficient and therefore results of transmembrane potential distributions and source current density distributions can be obtained in a time less than one hour on a common workstation. The calculation time of the Body Surface Potential Maps strongly depends on the spatial resolution of the volume conductor model and the temporal resolution of the source current density distributions. Depending on the desired quality calculation times of 1 hour up to several days can be reached. Current and future research is focussed on the influence of motion, the validation of the cellular automaton with animal experiments as well as on the simulation of surgical interventions by means of haptical interfaces. Efforts to match the model of the Visible Man data on patient data sets showed already good results [43]. Nonetheless, research will also focus on this topic to improve the developed methods.

Acknowledgements

This work is supported in parts by SFB 414 "Information Technology in Medicine: Computer- and Sensor-based Surgery", a co-operation between the University of Karlsruhe, the University of Heidelberg and the German Cancer Research Center (DKFZ).

References

- [1] A. L. Bardou, P. M. Auger, P. J. Birkui, and J.-L. Chassé, "Modeling of cardiac electrophysiological mechanisms: From action potential genesis to its propagation in myocardium," *Critical Reviews in Biomedical Engineering*, vol. 24, pp. 141-221, 1996.
- [2] M. J. Ackerman, "Viewpoint: The Visible Human Project," Journal Biocommunication, vol. 18, no. 2, p. 14, 1991.
- [3] V. Spitzer, M. J. Ackerman, A. L. Scherzinger, and D. Whitlock, "The Visible Human male: A technical report," *Journal of the American Medical Informatics Association*, vol. 3, no. 2, pp. 118-130, 1996.
- [4] W. Bargmann, "Bau des Herzens," in *Das Herz des Menschen* (W. Bargmann and W. Doerr, eds.), pp. 88-164, Stuttgart: Georg Thieme Verlag, 1963.
- [5] E. Bauereisen, "Normale Physiologie des Herzens," in *Das Herz des Menschen* (W. Bargmann and W. Doerr, eds.), ch. 7, pp. 313-354, Stuttgart: Georg Thieme Verlag, 1963.
- [6] T. H. Schiebler and W. Doerr, `Orthologie des Reizleitungssystems," in *Das Herz des Menschen* (W. Bargmann and W. Doerr, eds.), ch. 4, pp. 165-227, Stuttgart: Georg Thieme Verlag, 1963.
- [7] F. B. Sachse, C. Werner, M. Müller, and K. Meyer-Waarden, "Preprocessing of the Visible Man dataset for the generation of macroscopic anatomical models," in *Proc. First Users Conference of the National Library of Medicine's Visible Human Project*, pp. 123-124, 1996.
- [8] F. B. Sachse, M. Glas, M. Müller, and K. Meyer-Waarden, ``Segmentation and tissue-classification of the Visible Man dataset using the computertomographic scans and the thin-section photos," in *Proc. First Users Conference of the National Library of Medicine's Visible Human Project*, pp. 125-126, 1996.
- [9] F. B. Sachse, M. Wolf, C. Werner, and K. Meyer-Waarden, "Ein Leitfähigkeitsmodell des menschlichen Körpers unter Berücksichtigung der Anisotropie von Muskelgewebe," in 31. Jahrestagung der Dt. Gesellschaft f. Biomed. Technik, 1997.
- [10] F. B. Sachse, Modelle des menschlichen Körpers zur Berechnung von physikalischen Feldern. Aachen: Shaker, 1998.
- [11] F. B. Sachse, C. Werner, K. Meyer-Waarden, and O. Dössel, "Applications of the visible man dataset in electrocardiology: Calculation and visualization of body surface potential maps of a complete heart cycle," in *Proc. Second Users Conference* of the National Library of Medicine's Visible Human Project, pp. 47-48, 1998.

- [12] C. D. Werner, M. Müller, F. B. Sachse, and K. Meyer-Waarden, "Vorverarbeitung des Visible Man Datensatzes," in *Biomedizische Technik*, vol. 41, pp. 602-603, 1996.
- [13] R. C. Gonzalez and R. E. Woods, *Digital Image Processing*. Reading, Massachusetts; Menlo Park, California: Addison-Wesley, 1992.
- [14] N. Arad and D. Reisfeld, "Image warping using few anchor points and radial functions," *Computer Graphics Forum*, vol. 14, no. 1, pp. 35-46, 1995.
- [15] F. B. Sachse, M. Wolf, C. Werner, and K. Meyer-Waarden, "Extension of anatomical models of the human body: Three dimensional interpolation of muscle fiber orientation based on restrictions," *Journal of Computing and Information Technology*, vol. 6, no. 1, pp. 95-101, 1998.
- [16] J. Sobotta, Atlas der Anatomie des Menschen, vol. 2. Urban & Schwarzenberg, 20 ed., 1993.
- [17] F. H. Netter, Atlas der Anatomie des Menschen. Stuttgart; New York: Thieme, 1997.
- [18] T. H. Cormen, C. E. Leiserson, and R. L. Rivest, Introduction to Algorithms. Cambridge/Massachusetts: The MIT Press, 1990.
- [19[] E. W. Dijkstra, A Discipline of Programming. Englewood Cliffs/NJ: Prentice Hall, 1976.
- [20] M. R. Boyett, A. Clough, J. Dekanski, and A. V. Holden, "Modelling cardiac excitation and excitability," in *Computational Biology of the Heart* (A. Panfilov and A. V. Holden, eds.), ch. 1, pp. 1-48, Chichester: John Wiley & Sons, 1997.
- [21] J. Malmivuo and R. Plonsey, Bioelectromagnetism. New York; Oxford: Oxford University Press, 1995.
- [22] R. F. Schmidt and G. Thews, Physiologie des Menschen. Berlin; Heidelberg; New York: Springer, 25 ed., 1993.
- [23] A. L. Hodgkin and A. F. Huxley, "A quantitative description of membrane current and its application to conduction and excitation in nerve," *J. Physiol*, vol. 177, pp. 500-544, 1952.
- [24] G. W. Beeler and H. Reuter, "Reconstruction of the action potential of ventricular myocardial fibres," J. Physiol., vol. 268, pp. 177-210, 1977.
- [25] C.-H. Luo and Y. Rudy, "A model of the ventricular cardiac action potential," Circ Res., vol. 68, no. 6, pp. 1501-1526, 1991
- [26] M. S. Jafri, J. J. Rice, and R. L. Winslow, "Cardiac Ca^{2+} dynamics: The roles of ryanodine receptor adaptation and sarcoplasmic reticulum load," *Biophysical J*, vol. 74, pp. 1149-1168, Mar. 1998.
- [27] P. Wach, R. Killmann, F. Dienstl, and C. Eichtinger, "A computer model of human ventricular myocardium for simulation of ECG, MCG, and activation sequence including reentry rhythms," *Basic Research in Cardiology*, vol. 84, no. 4, 1989.
- [28] A. L. Bardou, P. M. Auger, R. Seigneuric, and J.-L. Chassé, ``Cellular automata models and cardiac arrythmias," in *Cellular Automata* (M. Delorme and J. Mazoyer, eds.), ch. 1, pp. 5-49, Dordrecht: Kluwer, 1999.
- [29] R. Killmann, P. Wach, and F. Dienstl, "Three-dimensional computer model of the entire human heart for simulation of reentry and tachycardia: Gap phenomenon and Wolff-Parksinson-White syndrome," *Basic Research in Cardiology*, vol. 86, no. 5, 1991.
- [30] B. E. H. Saxberg and R. J. Cohen, "Cellular automata models of cardiac conduction," in *Theory of Heart* (L. Glass, P. Hunter, and A. McCulloch, eds.), pp. 437-476, Berlin, Heidelberg, New York: Springer, 1991.
- [31] D. Wei, O. Okazaki, K. Harumi, E. Harasawa, and H. Hosaka, "Comparative simulation of excitation and body surface electrocardiogram with isotropic and anisotropic computer heart models," *IEEE Transactions on Biomedical Engineering*, vol. 42, pp. 343-357, Apr. 1995.
- [32] P. Siregar, J. P. Sinteff, N. Julen, and P. L. Beux, ``An interactive 3D anisotropic cellular automata model of the heart," *Computers and Biomedical Research*, vol. 31, pp. 323-347, 1998.
- [33] C. D. Werner, F. B. Sachse, and O. Dössel, "A computer simulation of pathological electrical excitation propagation in the human heart," in *Proc. EMBEC 99*, pp. 1632-1633, 1999.
- [34] M. Delorme, "An introduction to cellular automata," in *Cellular Automata* (M. .Delorme and J. Mazoyer, eds.), ch. 1, pp. 5-49, Dordrecht: Kluwer, 1999.
- [35] T. A. Sudkamp, Languages and Machines. Reading, Massachusetts; Menlo Park, California: Addison-Wesley, 2 ed., 1997.
- [36] D. B. Geselowitz, "On the theory of the electrocardiogram," Proceedings of the IEEE, vol. 77, pp. 857-876, June 1989.
- [37] C. S. Henriquez, A. L. Muzikant, and C. K. Smoak, "Anisotropy, fiber curvature and bath loading effects on activation in thin and thick cardiac tissue preparations: Simulations in a three-dimensional bidomain model," *J Cardiovascular Electrophysiology*, vol. 7, pp. 424-444, May 1996.
- [38] W. H. Press, S. A. Teukolsky, W. T. Vetterling, and B. P. Flannery, *Numerical Recipes in C.* Cambridge, New York, Melbourne: Cambridge University Press, 2 ed., 1992.
- [39] F. B. Sachse, C. Werner, K. Meyer-Waarden, and O. Dössel, "Comparison of solutions to the forward problem in electrophysiology with homogeneous, heterogeneous and anisotropic impedance models," in *Biomedizinische Technik*, vol. 42, pp. 277-280, 1997.
- [40] F. B. Sachse, C. D. Werner, K. Meyer-Waarden, and O. Dössel, "Development of a human body model for numerical calculation of electrical fields," in *Computerized Medical Imaging and Graphics*, vol. 24, pp. 165-171, 2000.

- [41] R. Klinge and S. Klinge, Praxis der EKG-Auswertung. Stuttgart, New York: Georg Thieme, 4 ed., 1996.
- [42] F. B. Sachse, C. D. Werner, and O. Dössel, "Techniken zur Visualisierung der elektrischen Aktivität des Herzens," in *Bildverarbeitung für die Medizin* (H. Evers, G. Glombitza, T. Lehmann, and H.-P. Meinzer, eds.), pp. 427-431, Berlin Heidelberg New York: Springer, 1999.
- [43] C. D. Werner, F. B. Sachse, and O. Dössel, "Simulation der elektrischen Erregung im Herzen auf Patientendatensätzen," in *Bildverarbeitung für die Medizin* (A. Horsch and T. Lehmann, eds.), pp. 287-291, Berlin Heidelberg New York: Springer, 2000.
- [44] K. Simelius, F. J. Nenonen, R. Hren, and B. Horacek, "Anisotropic propagation model of ventricular myocardium" *International Journal of Bioelectromagnetism*, vol. 2, no. 2, 2000.



Official journal of the International Society for Bioelectromagnetism